Supporting Information – Hybrid–2D Excitonic Metasurfaces for Complex Amplitude Modulation

Tom Hoekstra[1], Mark L. Brongersma[2], and Jorik van de Groep[1*]

[1] *Van der Waals-Zeeman Institute, Institute of Physics, University of Amsterdam, 1098 XH, Amsterdam, the Netherlands*
[2] *Geballe Laboratory for Advanced Materials, Stanford University, Stanford, CA 94305, USA*

[*] j.vandegroep@uva.nl

This file includes:

- Materials and methods
- Supplementary Notes 1-2
- Supplementary Figures 1-12

Materials and methods

Experimental

Sample fabrication. We manually exfoliate bulk hBN and WS_2 crystals (HQ Graphene) using Nitto SPV-224 tape. The exfoliated flakes are transferred onto stamps cut from polydimethylsiloxane (Gel-Pak WF-30). Using a custom-built microscope with a transfer stage and heating element (Thorlabs), we identify suitable multilayer hBN and monolayer WS_2 flakes on the stamps. Next, we place a diced 12×12 mm^2 Si substrate with 100 nm dry-grown thermal oxide (University Wafer) on the heating stage with a restickable adhesive dot (Scotch). We mount the stamp with the bottom hBN flake on the transfer stage, align it to the substrate, and bring it into contact at ambient conditions (T = 21 °C, R.H. = 50%). The stage is then heated to 65 °C and allowed to thermalize for 5 minutes, after which we peel the stamp at a controlled rate of 0.5 μm/s to complete the transfer. We repeat this process sequentially for the WS_2 monolayer and the top hBN layer (thermalizing for 15 minutes in each case) to assemble the full heterostructure. Finally, we anneal the sample at 200 °C in vacuum (P ≈ 10^{-6} mbar) for 2 hours to promote adhesion and remove residues.

Cryogenic reflectance. We perform cryogenic reflectance measurements using a Montana CryoAdvance-50 cryostat, helium-cooled to 3 K, integrated with a custom-built 4f Köhler-illumination microscope (Thorlabs). The sample is illuminated with unpolarized white LED light through a 100× objective (Zeiss Epiplan-Neofluar, NA = 0.9). The reflected signal is collected with the same objective and focused onto the slit of a Princeton Instruments SpectraPro 2300i spectrometer, where it is chromatically dispersed (300 lines/mm) and recorded on a Pixis Si CCD camera (cooled to –70 °C).

Numerical fitting. We extract the resonance energy and linewidth of the A-exciton at 3 K by fitting the measured reflectance spectra. Because the exact heterostructure geometry is not known with sufficient precision, we analyze the reflectance contrast between the full stack (R_{sample}) and the bare substrate (R_{sub}), defined as $\Delta R/R_{\text{sub}} = (R_{\text{sample}} - R_{\text{sub}})/R_{\text{sub}}$. We compute $(\mathrm{d}/\mathrm{d}E)(\Delta R/R_{\text{sub}})$ in the relevant spectral window and fit it with the derivative of the Cauchy-Lorentz distribution to obtain the excitonic parameters (Supplementary Fig. S3). To account for spatial inhomogeneity in the sample, we repeat this procedure for 26 consecutive lines of the CCD image and report the average extracted parameters in the manuscript.

Numerical simulations

Inverse design. We develop a Python-based inverse design routine for parameter optimization in both the RCWA and TCMT simulations. For the RCWA simulations, we optimize the metasurface geometries (grating period, duty cycle, hBN thicknesses; all rounded to 0.1 nm increments) and the operating wavelength to achieve π-phase modulation, full complex amplitude modulation, and beam steering. For TCMT analysis, we use the same framework to optimize the operating wavelength, GMR resonance wavelength, and the exciton-photon coupling strengths. The optimization proceeds in two stages: an initial global search using Bayesian optimization (*scikit-optimize*) followed by local refinement with the covariance matrix adaptation evolution strategy (*pycma*). The accessible carrier densities and thus the bounds on the exciton non-radiative decay rate are set by the maximum applied gate voltages (5 V for the π-phase modulator, 10 V for the 2π modulator). For the π-phase modulator, we compute two complex reflection coefficients at intrinsic and strong n-type doping and define an objective function that maximizes the mean amplitude while minimizing both the amplitude variation and the deviation from a perfect π-phase shift. For the 2π-phase modulator, we evaluate a grid of reflection coefficients over the allowed carrier densities (n_t, n_b), and the objective function maximizes the angular coverage in the complex plane above a minimum amplitude while minimizing the amplitude variation across angles. Full objective-function definitions and algorithmic details are provided in Supplementary Note 1.

Rigorous coupled-wave analysis. Electromagnetic simulations of the metasurfaces are performed using the open-source Python implementation of S^4 RCWA[1], with circular lattice truncation and 561 Fourier orders to provide convergence (mean absolute deviation < 0.1%) while maintaining reasonable computation times. All computationally intensive tasks, such as inverse-design parameter optimization and high-resolution simulation runs, are executed on a self-hosted 64-core computing cluster. The frequency-dependent refractive indices of Ag, hBN and graphene are taken from literature as tabulated

data[2–4]. The permittivity of monolayer WS_2 is described by a Lorentz-oscillator model consisting of a background term to account for higher-order resonances and a sum of oscillators corresponding to the exciton resonances, each parametrized by the resonance energy, oscillator strength and total decay rate[5]. In this work, the A-exciton is the only relevant feature in the spectral region of interest. We use the resonance energy and intrinsic decay rate extracted from the cryogenic reflectance fits. The variation of γ_A with the carrier density is obtained with an optical rate equation model based on previous work[6,8].

Coupled mode theory. We use TCMT to evaluate the fundamental limits of phase modulation. First, to extract the GMR loss rates for each metasurface, we use RCWA to simulate their responses in the absence of excitons (setting $\gamma_{A,r} = 0$ meV) and fit the resulting spectra with a one-port, single-oscillator TCMT model. For the π-phase modulator, we construct a two-oscillator system consisting of the GMR and a single exciton resonance. The exciton's resonance energy and intrinsic decay rates are fixed from cryogenic fits, while its non-radiative linewidth under n-type doping is constrained by the maximum carrier density in the RCWA simulations. Using these parameters, together with the fitted GMR loss rates and the physically motivated upper bound on the coupling strength[6], we employ our inverse-design framework (Supplementary Note 1) to determine the maximum achievable reflection amplitude compatible with π-phase modulation (Supplementary Fig. S4). We apply the same procedure to the full 2π complex-amplitude modulator by extending the TCMT system to three coupled oscillators, with the third oscillator representing excitons in the second monolayer (Supplementary Fig. S9). To assess the impact of the fundamental loss channels on phase modulation, we co-optimize the radiative and non-radiative rates of the excitonic and guided-mode resonators and evaluate the resulting modulation depth (Supplementary Figs. S5 and S9). Full TCMT formulations are provided in Supplementary Note 2.

Carrier density calculations. We model the gated devices as a parallel-plate capacitor to relate the applied gate voltage to the 2D electron density. The geometric capacitance per unit area is $C_{geo} = \varepsilon_0\varepsilon_{hBN}/d_{hBN}$, with d_{hBN} the hBN thickness and ε_{hBN} its static permittivity. To account for the finite density of states in monolayer WS_2, we include the quantum capacitance of a 2D electron gas, $C_q = e^2 g_s g_v m^*/(\pi\hbar^2)$, where e is the elementary charge, m^* is the effective electron mass, and g_v and g_s are the valley and spin degeneracies, respectively[9,10]. The overall capacitance per unit area is given by the series combination $C = (1/C_{geo} + 1/C_q)^{-1}$.

Supplementary Note 1. Inverse design of hybrid-2D metasurfaces.

Throughout this work, parameter optimization is performed using an inverse design framework implemented in custom Python scripts. The target optical response is encoded in an objective function, *i.e.*, the figure-of-merit (FOM), and the optimization seeks the set of parameters that minimizes the FOM. This requires computationally efficient algorithms to navigate high-dimensional parameter spaces and accommodate multiple objectives. Broadly, optimization strategies fall into two categories: gradient-based and gradient-free[11]. Because the S^4 implementation of RCWA does not provide direct access to analytical gradients, we employ derivative-free techniques in this study.

Gradient-free optimization is well suited for electromagnetic design with a modest number of parameters. Although the absence of gradients typically slows convergence relative to gradient-based methods, these approaches are less sensitive to initialization. Here, we combine two complementary schemes: Bayesian optimization (implemented with *scikit-optimize*) for sample-efficient global exploration, followed by covariance matrix adaptation evolution strategy (CMA-ES, via *pycma*) for local refinement. Bayesian optimization constructs a Gaussian-process surrogate of the objective and focuses expensive evaluations on promising regions of parameter space. This is particularly beneficial for 2D periodic RCWA simulations where convergence requires many Fourier orders N and the simulation time scales as N^3. Once a promising region in parameter space is identified, CMA-ES is employed to refine the solution. CMA-ES is a stochastic, population-based evolutionary algorithm that iteratively adapts a Gaussian distribution over design candidates, requiring minimal manual hyper-parameter tuning which makes it straightforward to deploy.

(1) Metasurface for π-phase modulation

For the π-phase modulation metasurface with one monolayer, two complex reflection coefficients, r_i and r_n, are calculated at intrinsic and strong n-type doping, respectively. The optimization minimizes both the deviation from a perfect π-phase shift and amplitude variation, while maximizing the mean amplitude:

$$\mathrm{FOM} = w_1 \frac{|\Delta\phi - \pi|}{\pi} + w_2 \big||r_\mathrm{i}| - |r_\mathrm{n}|\big| - w_3 \frac{|r_\mathrm{i}| + |r_\mathrm{n}|}{2},$$

$$\Delta\phi = |\arg(r_\mathrm{i}) - \arg(r_\mathrm{n})|\,.$$

Here, $w_1 = 9$, $w_2 = 3$, and $w_3 = 1$ are the weights given to each sub-objective. For the RCWA optimization, the free parameters are the grating period Λ, grating element width w, grating height h, hBN thickness d, operating wavelength λ and carrier density in the n-doped state n_e. On the other hand, for the TCMT analysis, the free parameters are the operating energy E, GMR energy E_G, and coupling strength g.

(2) Metasurface for complex amplitude modulation

Next, for the complex-amplitude modulation metasurface with two monolayers, the complex reflection coefficient is sampled over the 2D carrier density space ($n_{e,\mathrm{top}}$, $n_{e,\mathrm{bot}}$) in the top and bottom monolayers:

$$r_{ij} \equiv r\left(n_{e,top}^{i}, n_{e,bot}^{j}\right).$$

The FOM aims to reward uniform phase coverage and maximize the amplitude over all phases. To quantify the phase coverage, we partition the interval [–π, π] into M uniform angular bins ϕ_m with:

$$\phi_m = -\pi + m\Delta\phi,$$

$$\Delta\phi = \frac{2\pi}{M}.$$

For each bin, we consider all grid points $\phi_{ij} = \arg(r_{ij})$ whose phase lies in that bin and whose amplitude exceeds a fixed threshold $|r|_{\min}$:

$$\mathcal{K}_m = \{(i,j) \,|\, \phi_{m-1} < \phi_{ij} < \phi_m,\ |r_{ij}| \geq |r|_{\min}\}.$$

We then define the maximum achievable amplitude in bin m as:

$$A_m = \begin{cases} \max\limits_{(i,j)\in\mathcal{K}_m} |r_{ij}|, & \text{If } \mathcal{K}_m \neq \emptyset, \\ 0, & \text{If } \mathcal{K}_m = \emptyset. \end{cases}$$

Finally, a scalar metric is extracted to describe the phase coverage:

$$C = \frac{1}{M}\sum_{m=1}^{M} \Theta(A_m),$$

where Θ is the Heaviside step function (a bin is "covered" if $A_m > 0$).

In addition, we maximize the minimum achievable amplitude across all phases:

$$A^*_{\min} = \min_{1\leq m\leq M} A_m\,.$$

Crucially, this definition of $A^*_{\min}$ ensures full phase coverage before optimizing the amplitude, because if at least one bin remains unpopulated, $A^*_{\min} = 0$. In other words, this definition treats the lowest achievable amplitude across the full 0–2π phase range as the limiting factor. This ensures that the metasurface maintains a usable reflection amplitude for all phases, which is a prerequisite for complex amplitude modulation.

With these definitions, we calculate the FOM as:

$$\text{FOM} = -w_1 \text{C} - w_2 A^*_{\min},$$

where we choose weights $w_1 = w_2 = 1$. In the RCWA simulations, we optimize this FOM for the following free parameters: grating period Λ, grating element width w, grating height h, top hBN thickness d_{top}, bottom hBN thickness d_{bot}, and operating wavelength λ. In the TCMT analysis, the free parameters are the operating energy E, GMR energy E_G, and coupling strengths with top and bottom monolayer g_{top} and g_{bot}, respectively.

(3) Three-level programmable metasurface for beam steering

Lastly, we leverage the complex amplitude modulator to demonstrate a three-level programmable beam steering metasurface. Here, we denote with R_k the reflected power (normalized to incident power) in diffraction order k, and R_{tot} is the total reflected power. For beam-steering design 'Configuration A', we target the –1 diffraction order, and define the diffraction efficiency as:

$$\eta_{-1} = \frac{R_{-1}}{R_{\text{tot}}}\,.$$

The objective function is given by:

$$\text{FOM} = -w_1\eta_{-1} - w_2 R_{-1},$$

with weights $w_1 = 1$ and $w_2 = 3$. This favors both a high fraction of power into the steered order as well as a large absolute value of that power, preventing the optimizer from converging to trivial solutions with high relative efficiency but negligible absolute power. In our RCWA simulations, the grating element width w is the only geometric parameter that is re-optimized. We further optimize the operating wavelength λ, and a pair of ($n_{e,\text{top}}$, $n_{e,\text{bot}}$) for each of the three unit cells within the supercell.

Supplementary Note 2. Temporal coupled mode theory analysis of coupling between excitonic and photonic resonances.

We employ a temporal coupled mode theory (TCMT) analysis to study the fundamental limits of π-phase and complex-amplitude modulation with hybrid-2D metasurfaces. To achieve this, we first obtain the loss rates of the guided mode resonance (GMR, denoted by subscript G) by performing RCWA simulations of the metasurfaces without excitons. Since the metasurfaces can only be addressed from the top side, we describe this system with a one-port one-oscillator TCMT model. The temporal evolution of the mode amplitude, a_G, driven by the incident field S_{in}, is given by:

$$\frac{da_G}{dt} = (-i\Delta_G + \Gamma_G)\, a_G + \sqrt{2\Gamma_{G,r}}\, S_{in},$$

where Δ_G is the detuning between photon energy ω and resonance energy ω_G, and Γ_G is the damping rate (amplitude decay rate, or half-width-at-half-maximum, $\Gamma = \gamma/2$) with radiative component $\Gamma_{G,r}$. The corresponding input-output relation for a one-port resonator is given by:

$$S_{out} = -r_{bg} S_{in} + \sqrt{2\Gamma_{G,r}}\, a_G,$$

where r_{bg} is a constant that accounts for a slowly varying background reflection term. In the steady state, solving the coupled equations for a_G and substituting into the input-output relation yields the reflection coefficient, defined as $r = S_{out}/S_{in}$:

$$a_G = \left(\frac{\sqrt{2\Gamma_{G,r}}}{-i\Delta_G + \Gamma_G}\right) S_{in},$$

$$r(\omega) = -r_{bg} + \frac{2\Gamma_{G,r}}{-i\Delta_G + \Gamma_G}.$$

From this procedure, for the metasurface with one monolayer, we find $\Gamma_{G,r}$ = 27.5 meV and $\Gamma_{G,nr}$ = 6.9 meV for the radiative and non-radiative components, respectively. For the metasurface with two monolayers, the non-radiative damping rate increases to $\Gamma_{G,nr}$ = 9.3 meV.

With these rates locked in, we now add the excitons back into the model. We first consider the metasurface with one monolayer and thus a single exciton resonance (denoted with subscript A) coupled to the GMR (Supplementary Fig. S4). The intrinsic exciton resonance energy ω_A and damping rate Γ_A are obtained by fitting the reflectance of hBN-encapsulated WS_2 measured at 3 K (Supplementary Fig. S3). The evolution of Γ_A with the carrier density n_e in monolayer WS_2 is taken from our previous work[6]. Since, in our system, $\Gamma_{G,r} \gg \Gamma_{A,r}$ and the exciton-GMR coupling strength g typically exceeds $\Gamma_{A,r}$ by roughly an order of magnitude, we assume that optical coupling from free space is mediated entirely by the metasurface, and therefore neglect direct coupling between excitons and free-space[6,12]. In the steady state, the coupled equations are then written as:

$$\frac{d}{dt}\begin{pmatrix} a_G \\ a_A \end{pmatrix} = \begin{pmatrix} -i\Delta_G + \Gamma_G & -ig \\ -ig & -i\Delta_A + \Gamma_A(n_e) \end{pmatrix}\begin{pmatrix} a_G \\ a_A \end{pmatrix} + \begin{pmatrix} \sqrt{2\Gamma_{G,r}} \\ 0 \end{pmatrix} S_{in}.$$

Solving this system, we find that the reflection coefficient is described as:

$$r(\omega) = -r_{bg} + \frac{2\Gamma_{G,r}}{-i\Delta_G + \Gamma_G + \frac{g}{-i\Delta_A + \Gamma_A(n_e)}}.$$

Finally, we consider the metasurface with two monolayers (Supplementary Fig. S9), 'top' and 'bottom', with exciton resonances described by the same resonance frequency ω_A, but unique decay rates $\Gamma_{A,top}(n_{e,top})$ and $\Gamma_{A,bot}(n_{e,bot})$, as well as coupling rates g_{top} and g_{bot}. Since, in practice, both monolayers

are separated by a tens-of-nanometers-thick hBN layer, the coupling between the two exciton resonances can be ignored. This gives a three-oscillator TCMT model with the following coupled equations:

$$\frac{d}{dt}\begin{pmatrix} a_{\mathrm{G}} \\ a_{\mathrm{A,top}} \\ a_{\mathrm{A,bot}} \end{pmatrix} = \begin{pmatrix} -i\Delta_{\mathrm{G}} + \Gamma_{\mathrm{G}} & -ig_{\mathrm{A,top}} & -ig_{\mathrm{A,bot}} \\ -ig_{\mathrm{A,top}} & -i\Delta_{\mathrm{A}} + \Gamma_{\mathrm{A,top}}(n_{\mathrm{e,top}}) & 0 \\ -ig_{\mathrm{A,bot}} & 0 & -i\Delta_{\mathrm{A}} + \Gamma_{\mathrm{A,bot}}(n_{\mathrm{e,bot}}) \end{pmatrix} \begin{pmatrix} a_{\mathrm{G}} \\ a_{\mathrm{A,top}} \\ a_{\mathrm{A,bot}} \end{pmatrix} + \begin{pmatrix} \sqrt{2\Gamma_{\mathrm{G,r}}} \\ 0 \\ 0 \end{pmatrix} S_{\mathrm{in}},$$

and the reflection coefficient is:

$$r(\omega) = -r_{\mathrm{bg}} + \frac{2\Gamma_{\mathrm{G,r}}}{-i\Delta_{\mathrm{G}} + \Gamma_{\mathrm{G}} + \frac{g_{\mathrm{A,top}}^2}{-i\Delta_{\mathrm{A}} + \Gamma_{\mathrm{A,top}}(n_{\mathrm{e,top}})} + \frac{g_{\mathrm{A,bot}}^2}{-i\Delta_{\mathrm{A}} + \Gamma_{\mathrm{A,bot}}(n_{\mathrm{e,bot}})}}.$$

The closed-form analytic expressions for *r* of the two- and three-oscillator TCMT models provide valuable insight into the principles governing phase modulation, without relying on specific device geometries. In particular, for complex amplitude modulation it is not self-evident why two degenerate exciton resonances should uniquely impact the complex reflection amplitude. However, from the equation above it is clear that the symmetry between both resonances is broken when $g_{A,top} \neq g_{A,bot}$ (Supplementary Fig. S6). In addition, by modifying the fitted radiative and non-radiative rates, we can assess the ultimate limits of both π-phase modulation (Supplementary Fig. S5) and complex amplitude modulation (Supplementary Fig. S10).

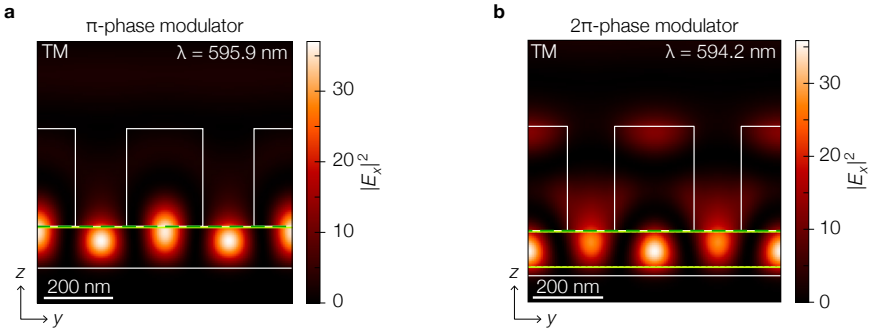

Supplementary Figure S1: Electric field profiles under transverse magnetic polarization. Electric field intensity ($|E_x|^2$) enhancement in absence of excitons, for a transverse magnetic (TM) polarized normal-incident wave **(a)** for the π-phase modulator at λ = 595.9 nm, and **(b)** for the 2π-phase modulator at λ = 594.2 nm. The positions of 1L WS_2 (light green, solid) and graphene (dark green, dashed) are indicated.

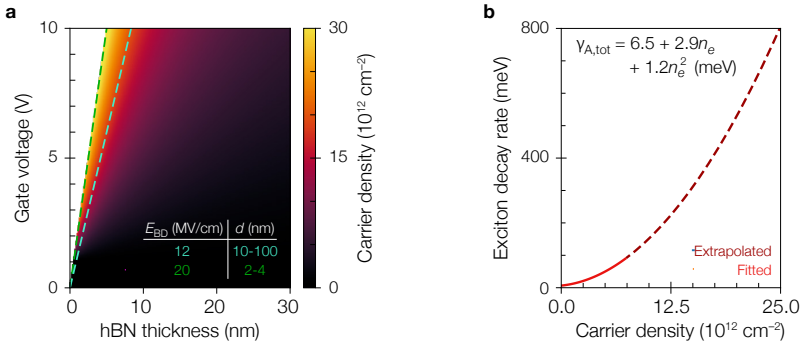

Supplementary Figure S2: Electrical tuning of exciton decay rate. (a) Gate-induced carrier density n_e in monolayer WS_2 calculated with a parallel-plate capacitor model modified to include the quantum capacitance, using hBN as gate dielectric. Two representative hBN breakdown field limits are indicated: $E_{BD} = 12^{13}$ and 20^{14} MV/cm for thicknesses d = 10-100 and 2-4 nm, respectively (green and cyan dashed lines). **(b)** Total A-exciton decay rate $\gamma_{A,tot}$ as function of n_e (fit: $\gamma_{A,tot} = 6.5 + 2.9n_e + 1.2n_e^2$ (meV) with n_e in units of 10^{12} cm^{-2}). The solid red curve is a fit to experimental data taken from previous work[6] up to $n_e = 7.3\times10^{12}$ cm^{-2}, the dashed maroon curve is extrapolated beyond this range.

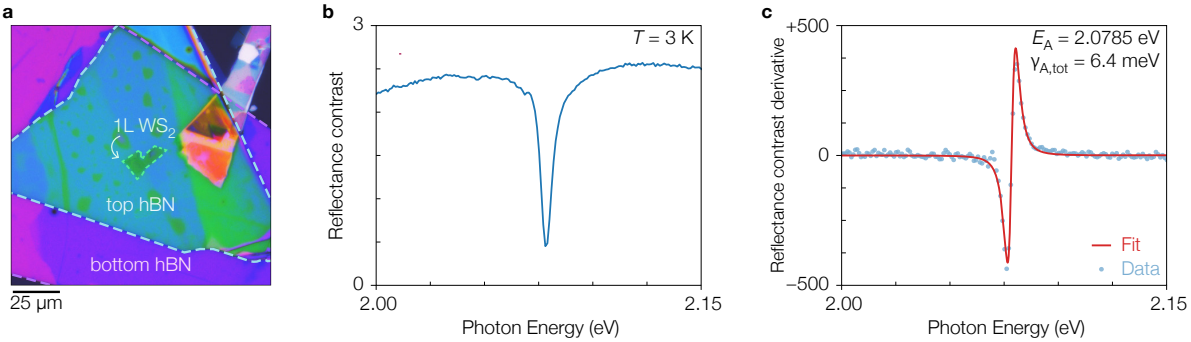

Supplementary Figure S3: Fitting exciton parameters from experimental reflectance. (a) Brightfield microscope image of the fabricated planar heterostructure sample, with monolayer (1L) WS_2 sandwiched between hBN. **(b)** Representative reflectance contrast spectrum of the sample with respect to the substrate, $(R_{sample} - R_{sub})/R_{sub}$, measured at T = 3 K. **(c)** Corresponding derivative of the reflectance contrast with respect to the photon energy (pale blue dots) and Lorentzian fit (red line) used to extract the total linewidth and center energy of the A-exciton resonance. The values reported in the main manuscript are the average of 23 similarly fitted spectra.

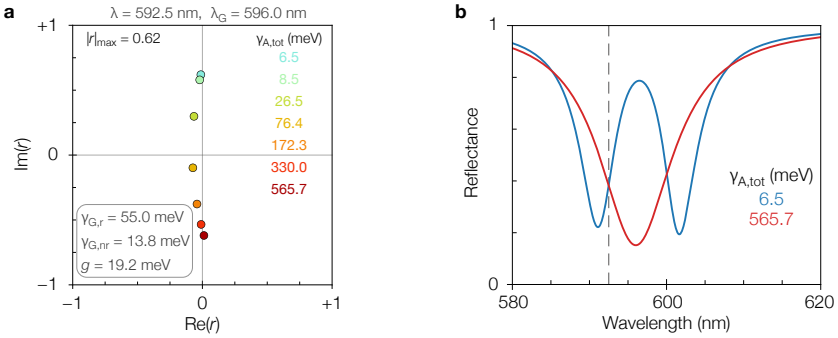

Supplementary Figure S4: Coupled mode theory analysis of a π-phase modulator. (a) Complex reflection coefficients of the optimized metasurface at operating wavelength λ = 592.5 nm for different values of the total exciton decay rate $\gamma_{A,tot}$ (indicated by color), calculated using coupled mode theory. The optimized metasurface achieves π-phase modulation at $|r|_{max}$ = 0.62 with these parameters: resonance wavelength λ_G = 596.0 nm, radiative linewidth $\gamma_{G,r}$ = 55.0 meV, non-radiative linewidth $\gamma_{G,nr}$ = 13.8 meV, exciton-photon coupling rate g = 19.2 meV. **(b)** Reflectance spectra at intrinsic (blue) and strong n-type doping (red) indicated by their respective exciton decay rates of $\gamma_{A,tot}$ = 6.5 and 565.7 meV. Dashed line indicates the operating wavelength.

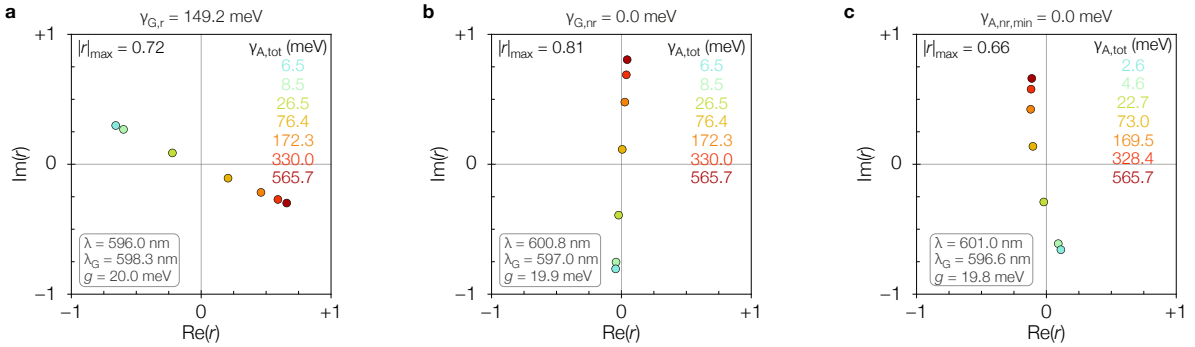

Supplementary Figure S5: Coupled mode theory analysis of the fundamental limits of π-phase modulation. The complex reflection coefficients calculated for different total exciton decay rates $\gamma_{A,tot}$ (colored dots). The optimized free parameters (operating wavelength λ, metasurface resonance wavelength λ_G, exciton-photon coupling strength g) are listed in the lower left corner of each diagram. The explored limiting cases are **(a)** optimal radiative coupling $\gamma_{G,r}$ = 149.2 meV ($|r|_{max}$ = 0.72), **(b)** absence of absorption losses $\gamma_{G,nr}$ = 0.0 meV ($|r|_{max}$ = 0.81), and **(c)** unity excitonic quantum yield at intrinsic doping $\gamma_{A,nr,min}$ = 0.0 meV ($|r|_{max}$ = 0.66).

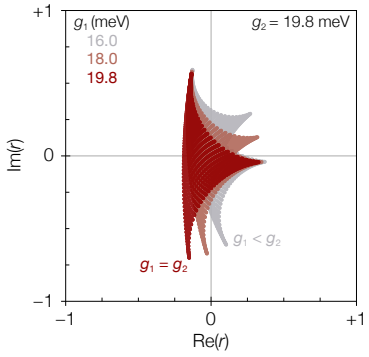

Supplementary Figure S6: Asymmetric reflection tunability through unequal coupling strengths. (a) Phasor diagram of the reflection coefficients r spanning the full tunable range of a 2π-phase modulator in three different scenarios, calculated using a three-oscillator temporal coupled-mode model. For equal coupling strengths g_1 = g_2 = 19.8 meV (dark red), the contribution of each exciton resonance is identical and their impact on r is fully symmetric. Reducing the coupling strength of one exciton to g_1 = 18.0 meV (orange) and g_1 = 16.0 meV (gray) breaks the symmetry and leads to the appearance of two distinct lobes in the complex plane.

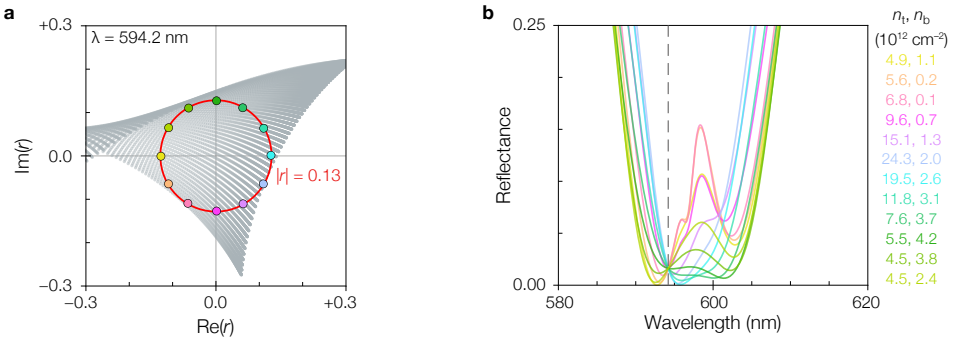

Supplementary Figure S7: Gate-dependent reflectance of the 2π-phase modulator. (a) Phasor diagram of the reflection coefficients, r, at λ = 594.2 nm (operating wavelength) for all allowed combinations of carrier densities in the top and bottom monolayers (n_t, n_b; gray dots). The red circle with $|r|$ = 0.13 indicates the constant-amplitude trajectory along which the reflection phase spans 2π, and twelve evenly spaced points on this circle (colored dots) represent selected r values. **(b)** Reflectance spectra corresponding to the colored points in (a), labeled with their respective (n_t, n_b) values. The operating wavelength is indicated (dashed line).

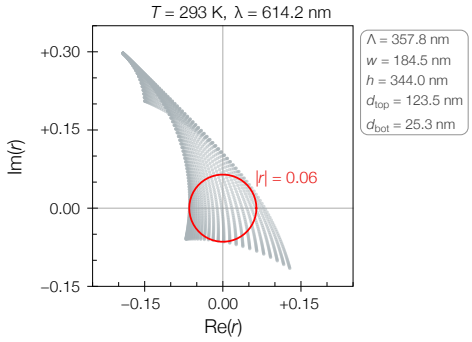

Supplementary Figure S8: Complex amplitude modulation at room temperature. Phasor diagram of the reflection coefficients, r, at λ = 614.2 nm for all allowed combinations of carrier densities in the top and bottom monolayers (gray dots), simulated at room temperature (T = 293 K). The optimized design achieves full 2π complex amplitude modulation at $|r|$ = 0.06 (red circle) with these parameters: grating period Λ = 357.8 nm, element width w = 184.5 nm, height h = 344.0 nm, and top and bottom hBN thicknesses d_{top} = 123.5 nm and d_{bot} = 25.3 nm, respectively.

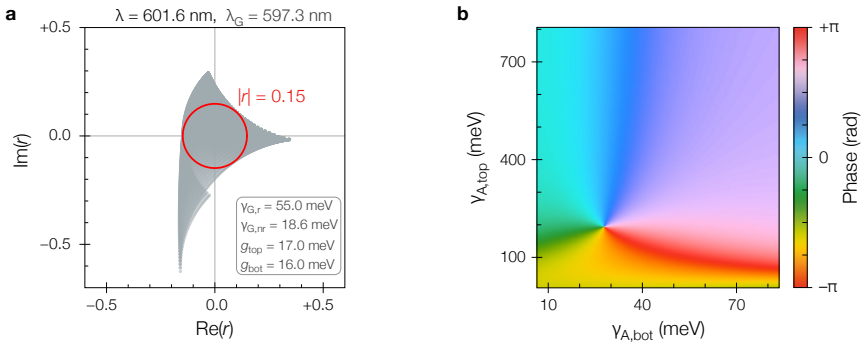

Supplementary Figure S9: Coupled mode theory analysis of a 2π-phase modulator. (a) Coupled mode theory calculation of the complex reflection coefficients of the optimized metasurface at operating wavelength λ = 601.6 nm for all allowed values of the exciton decay rates $\gamma_{A,top}$ and $\gamma_{A,bot}$ in the top and bottom monolayers, respectively (gray dots). The optimized design achieves full 2π phase modulation at $|r|$ = 0.15 (red circle) with these parameters: resonance wavelength λ_G = 597.3 nm, radiative linewidth $\gamma_{G,r}$ = 55.0 meV, non-radiative linewidth $\gamma_{G,nr}$ = 18.6 meV, and exciton-photon coupling rates g_{top} = 17.0 meV and g_{bot} = 16.0 meV. **(b)** Reflection-phase map as function of $\gamma_{A,top}$ and $\gamma_{A,bot}$ showing the phase singularity.

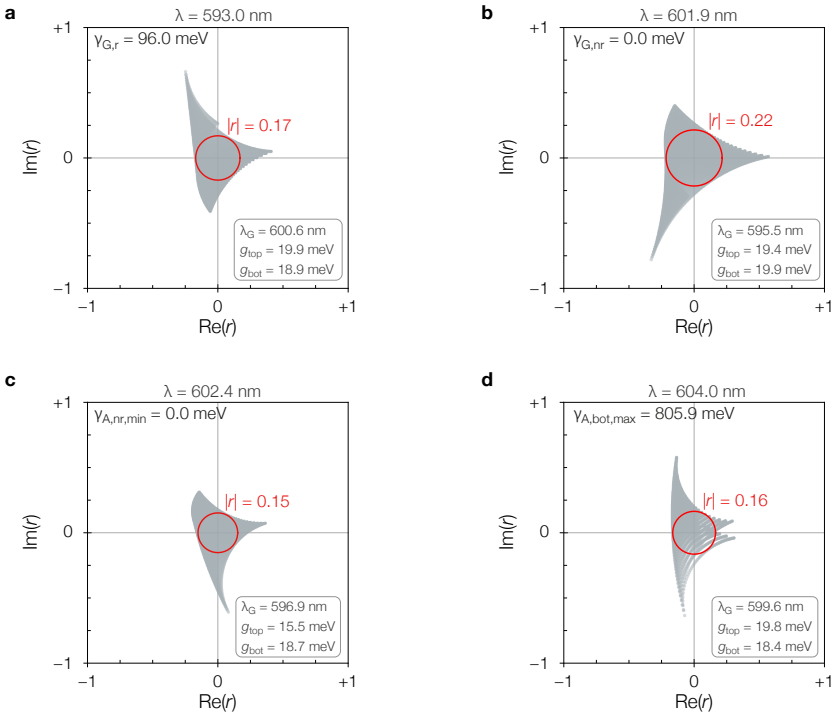

Supplementary Figure S10: Coupled mode theory analysis of the fundamental limits of 2π-phase modulation. The complex reflection coefficients calculated for all allowed values of the exciton decay rates $\gamma_{A,top}$ and $\gamma_{A,bot}$ in the top and bottom monolayers, respectively (gray dots). The red circles indicate the largest constant-amplitude trajectory along which the reflection phase spans the full 0–2π range. The optimized free parameters (operating wavelength λ, metasurface resonance wavelength λ_G, exciton-photon coupling strengths g_{top} and g_{bot}) are listed in the lower right corner of each diagram. The explored limiting cases are **(a)** optimal radiative coupling $\gamma_{G,r}$ = 96.0 meV ($|r|$ = 0.17), **(b)** absence of absorption losses $\gamma_{G,nr}$ = 0.0 meV ($|r|$ = 0.22), **(c)** unity excitonic quantum yield at intrinsic doping $\gamma_{A,nr,min}$ = 0.0 meV ($|r|$ = 0.15), and **(d)** full tuning range of excitons in bottom monolayer $\gamma_{A,bot,max}$ = 805.9 meV ($|r|$ = 0.16).

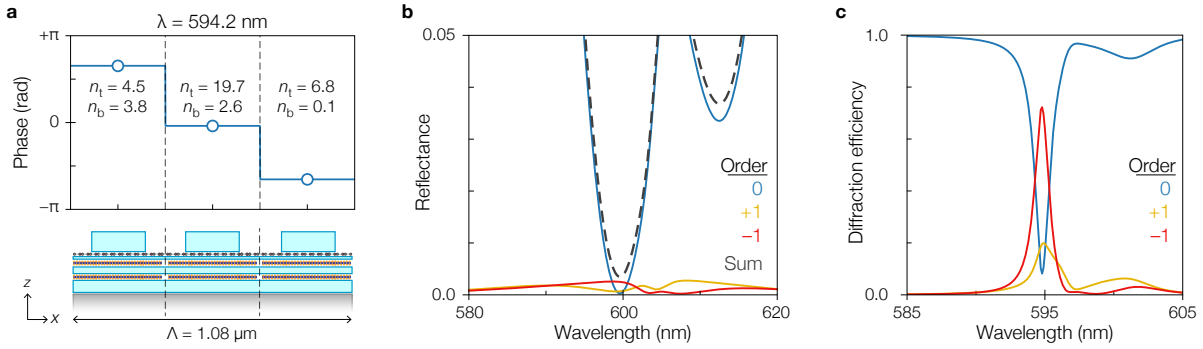

Supplementary Figure S11: Forward-designed beam steering metasurface. (a) Three-level programmable metasurface with supercell period Λ, designed for redirecting light at λ = 594.2 nm into the –1 order, with a constant phase gradient (top) achieved by tuning the top (n_t) and bottom (n_b) carrier densities to the values indicated (units: 10^{12} cm^{-2}) **(b)** Reflected power into the –1 (red), 0 (blue), and +1 (yellow) orders, with the total reflectance represented by the dashed line. **(c)** The corresponding diffraction efficiency reveals 72.2% of reflected power is redirected into the –1 order at λ = 594.8 nm.

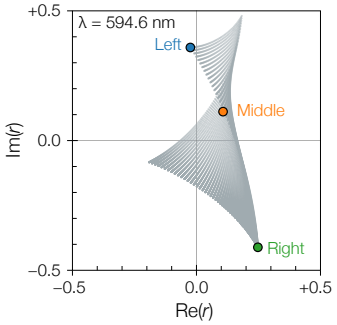

Supplementary Figure S12: Reflection coefficients of the designed three-level programmable metasurface. Phasor diagram of the reflection amplitudes and phases achievable for each unit cell of the three-level programmable metasurface. The reflection coefficients of the "left" (blue), "middle" (orange) and "right" (green) unit cells of Configuration A in Fig. 4a are highlighted.

References

1. Liu, V. & Fan, S. S^4: A free electromagnetic solver for layered periodic structures. *Computer Physics Communications* **183**, 2233–2244 (2012).
2. Ciesielski, A., Skowronski, L., Trzcinski, M. & Szoplik, T. Controlling the optical parameters of self-assembled silver films with wetting layers and annealing. *Applied Surface Science* **421**, 349–356 (2017).
3. Lee, S. Y., Jeong, T. Y., Jung, S. & Yee, K. J. Refractive Index Dispersion of Hexagonal Boron Nitride in the Visible and Near-Infrared. *Phys. Status Solidi B* **256**, 1800417 (2019).
4. El-Sayed, M. A. *et al.* Optical Constants of Chemical Vapor Deposited Graphene for Photonic Applications. *Nanomaterials* **11**, 1230 (2021).
5. Li, Y. *et al.* Measurement of the optical dielectric function of monolayer transition-metal dichalcogenides: MoS_2, $MoSe_2$, WS_2, and WSe_2. *Phys. Rev. B* **90**, 205422 (2014).
6. Hoekstra, T. & van de Groep, J. Electrically tunable strong coupling in a hybrid-2D excitonic metasurface for optical modulation. *Light Sci Appl* **15**, 28 (2026).
7. Wilson, J. A. & Yoffe, A. D. The transition metal dichalcogenides discussion and interpretation of the observed optical, electrical and structural properties. *Advances in Physics* **18**, 193–335 (1969).
8. Lien, D. H. *et al.* Electrical suppression of all nonradiative recombination pathways in monolayer semiconductors. *Science* **364**, 468–471 (2019).
9. Brumme, T., Calandra, M. & Mauri, F. First-principles theory of field-effect doping in transition-metal dichalcogenides: Structural properties, electronic structure, Hall coefficient, and electrical conductivity. *Phys. Rev. B* **91**, 155436 (2015).

10. Ma, N. & Jena, D. Carrier statistics and quantum capacitance effects on mobility extraction in two-dimensional crystal semiconductor field-effect transistors. *2D Mater.* **2**, 015003 (2015).
11. Elsawy, M. M. R., Lanteri, S., Duvigneau, R., Fan, J. A. & Genevet, P. Numerical Optimization Methods for Metasurfaces. *Laser & Photonics Reviews* **14**, 1900445 (2020).
12. Li, Q. *et al.* A Purcell-enabled monolayer semiconductor free-space optical modulator. *Nat. Photon.* **17**, 897–903 (2023).
13. Hattori, Y., Taniguchi, T., Watanabe, K. & Nagashio, K. Anisotropic Dielectric Breakdown Strength of Single Crystal Hexagonal Boron Nitride. *ACS Appl. Mater. Interfaces* **8**, 27877–27884 (2016).
14. Ranjan, A. *et al.* Dielectric Breakdown in Single-Crystal Hexagonal Boron Nitride. *ACS Appl. Electron. Mater.* **3**, 3547–3554 (2021).